EPJ Web of Conferences **346**, 03007 (2026) https://doi.org/10.1051/epjconf/202634603007
RFPPC2025

Direct Measurement of ICRF-Enhanced Plasma Potentials on WEST Using Reciprocating Emissive Probes

Raymond Diab[1*], *Seung-Gyou* Baek[1], *Laurent* Colas[2], *Benoit* Guillermin[2], *James-Paul* Gunn[2], *Tristan* Batal[2], *William* Burke[1], *Nicolas* Fedorczak[2], *Julien* Hillairet[2], *Rick* Leccacorvi[1], *Rui* Vieira[1], and the WEST Team

[1]MIT Plasma Science and Fusion Center, Cambridge, MA 02139, United States of America
[2]CEA, IRFM, F-13108 Saint-Paul-Lez-Durance, France

Abstract. An extensive documentation of ICRF-enhanced plasma potentials has been conducted over two experimental campaigns on the WEST tokamak using reciprocating emissive probes magnetically connected to two ICRF antennas. The collected data spans a wide range of antenna electrical settings (coupled power, toroidal phasing, left–right power balance) and plasma parameters (density at the antenna limiter above and below the lower hybrid resonance, plasma current, minority fraction). By scanning the edge safety factor across multiple probe plunges, the magnetic connection between the probe and the antenna varied, enabling the construction of a 2D map of the plasma and floating potentials around an active ICRF antenna. This dataset will be used to validate RF simulation tools equipped with the sheath boundary condition and used to predict RF rectified potentials and ICRF-induced impurity sputtering in future machines. This paper presents the diagnostic and some initial measurements, while the rest will be reported elsewhere.

1 Introduction

Due to the nonlinearity of the current-voltage (I-V) relationship of the plasma sheath, a radio frequency (RF) voltage will draw on average more electrons than ions towards the wall. To restore ambipolarity, the DC electrical potential of the plasma rises, slowing down electrons and accelerating ions to the wall, enhancing their sputtering yield. This phenomenon, known as RF sheath rectification, is responsible for enhanced impurity generation and antenna heat loads during ion cyclotron range of frequencies (ICRF) operation in magnetically confined fusion plasmas [1,2]. Despite the importance of the plasma potential in determining ICRF-induced impurity contamination, it is rarely measured directly in tokamaks. Several RF codes [3,4,5,6] now incorporate appropriate sheath boundary conditions [7], which enable predictions of the rectified sheath potential on ICRF antenna limiters and other plasma-facing components. However, these predictions have yet to be quantitatively validated against experimental data with realistic antenna geometry and plasma parameters. This project aims to fill this gap by assembling a database of plasma potential profiles around an active ICRF antenna in a tokamak environment under a wide range of operating conditions.

2 Diagnostic Description

To enable these measurements, a new reciprocating probe head was built at MIT and installed on WEST in late 2023. It is equipped with three emissive probes and two conventional Langmuir probes. A photo of the probe head inside the WEST vacuum vessel is shown in Figure 1(a). The heat shield is made entirely of TZM, a molybdenum alloy selected for its high melting point and thermal conductivity, relatively good machinability, and compatibility with WEST's full-metal environment. The Langmuir probes are arranged in the Mach configuration (one on each side of the probe head), while the three emissive probes are positioned on the same side of the probe head, magnetically connected to the Q1 and Q2 ICRF antennas, as shown in Figure 2. The side of the probe head where the emissive probes are located will be referred to hereafter as "side B", while the other side will be referred to as "side A". Side A corresponds to the electron side of the probe head, and side B to the ion side. The Langmuir probes are made of tantalum, chosen for its high melting point and ductility at room temperature, which allows for simple crimping of the probe tips to the cables inside the probe head. They were usually operated in swept mode, which enables measurements of the electron temperature, floating potential, ion saturation current, and parallel Mach number. The emissive probes consist of thin (0.125 mm) thoriated tungsten filaments, heated above 1800 °C by a 62.5 kHz AC current. Following the Alcator C-Mod experience [8], an AC drive was chosen to average out **J**×**B** forces on the filaments and extend their lifetime. The small amount of thorium (1%) lowers the work function of the filaments, increasing their electron emissivity. Each filament is housed in a MACOR enclosure and about 1/3 of it (the middle part, which reaches the highest temperatures when ohmically heated) faces the plasma through a slit on the side of the probe head.

* Corresponding author: diab@mit.edu

The emissive probes enable a direct measurement of the plasma potential in the far scrape-off layer (SOL), near the ICRF antenna, by emitting electrons to cancel the excess electron flux coming from the plasma. When the filaments operate in emissive mode, their floating potential should roughly equal the plasma potential. A low-pass filter eliminates high-frequency components from the signal. Hence, in this paper, "plasma potential" will refer more precisely to the DC component of the plasma potential, V_{DC}. Due to the filaments' fragility, the adopted strategy was to use only one filament most of the time and keep the others as backup. The probe plunges vertically from the top of the machine, reaching its maximum depth in about 250 ms before retracting to its garage position. Over two years of operation, the probe was plunged more than 300 times and withtook many plasma disruptions without substantial damage. The thermal and structural analysis of the probe head was presented in [9] and predicted safe margins for the probe's operation. In Figure 1(b), an infrared camera view of the probe head is shown during its plunge in a WEST plasma. The hot filament is clearly visible, as well as the tip of the probe head, which heats up as it intercepts fast electrons generated by lower hybrid waves and trapped in the magnetic ripple. The IR camera system could be used to remotely monitor whether the filament was broken, although its spatial resolution was insufficient to measure the filament temperature. The RMS heating current through the filament also provided a reliable indicator of filament integrity.

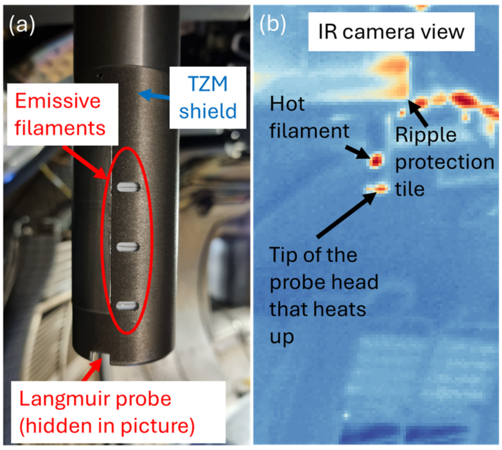

Fig. 1. (a) Picture of the TZM probe head inside the WEST vacuum vessel with the three emissive filaments visible on the side. (b) IR camera view of the probe head during its plunge in a WEST plasma with the hot emissive filament clearly visible.

As shown in Figure 2, the probe was magnetically connected to the top of the Q1 antenna, where large peaks in tungsten sputtering and heat fluxes are usually observed [10]. Magnetic connection to Q2 was also possible by retracting the Q1 antenna, though the plasma potential measured by the probe was usually much more sensitive to power from the Q1 antenna. This is because the probe typically connects magnetically to the middle of the Q2 antenna, where the rectified potential tends to be weaker (see, for example, Figure 12). That said, in some scenarios, large plasma potentials were still observed when only the Q2 antenna was powered (see, for example, Figure 9).

3 Initial Measurements

A typical plasma potential profile measured by our probe during ICRF power injection from the Q1 antenna is shown in Figure 3 and compared to a reference case without ICRF. The ICRF enhancement of the plasma potential is clearly visible. Also shown is the probe's depth with respect to its resting position at the top of the machine. Around a depth of 180 mm, the probe crosses the ripple protection tiles (see Figure 1(b)) and becomes magnetically connected to the antenna, hence the sharp increase in plasma potential at this location. As will be shown later, the large peak in plasma potential, measured here at a depth of about 325 mm, corresponds to those field lines that cross the leading edge of the ICRF antenna limiter. As the probe plunges in and out of the plasma, it records approximately the same profile twice.

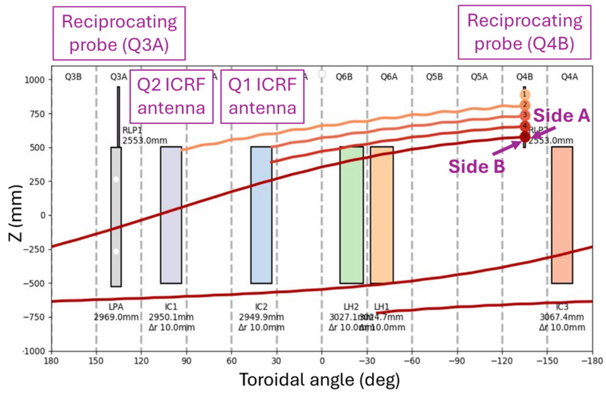

Fig. 2. Representation of the WEST outer wall showing the magnetic field line connections from the reciprocating emissive probe (in port Q4B) to the Q1 and Q2 ICRF antennas for the case studied in Figure 3. The location of the reciprocating Langmuir probe in port Q3A is also shown as it will be used for the analysis in Figure 12.

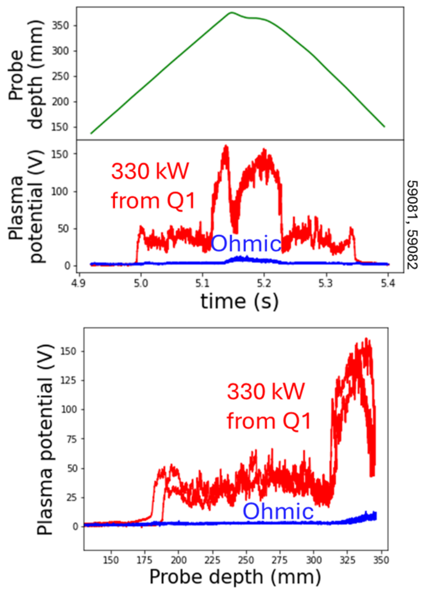

Fig. 3. In the top plot, the probe depth and plasma potential are shown as a function of time for a plunge in an ohmic plasma (blue) and in a plasma with 330 kW of ICRF power from the Q1 antenna (red) at $I_p = 500$ kA. In the bottom plot, the plasma potential profile is plotted against the probe depth, using data from the full in-and-out reciprocation. The Q2 antenna was not powered in these shots.

The floating potential of the hot (emissive) filament is always positive and bigger than that of the (non-emissive) cold filament and Langmuir probes, which can be either positive or negative, as shown in Figure 4. In most cases, only the Langmuir probe located on side B of the probe head (the same side as the emissive probes) shows a floating potential increase when the antennas are powered. This positive shift in the Langmuir probe's floating potential means that the electrically grounded electrode would collect a DC current at the probe position and suggests that the excess electron flux caused by the strong RF fields at the antenna is not fully compensated by plasma potential enhancement. Ambipolarity is therefore not satisfied locally, but on average over the entire wall. DC currents are allowed to flow in the plasma and vacuum vessel as long as they form closed circuits, and the shift in floating potential is indicative of those DC currents driven by the RF fields' interaction with the sheath [1,2]. The difference between the plasma and floating potentials is often (but not always) lower than the value of ~3T_e predicted by simple probe theory and can be as low as ~T_e, where T_e is the electron temperature at the probe's location. The same observation was made on Tore Supra, where the plasma potential was estimated using a retarding field analyzer [11,12]. This discrepancy could be explained by a high secondary electron emission yield, which was clearly evidenced on Tore Supra [13] and is often neglected when interpreting Langmuir probe measurements.

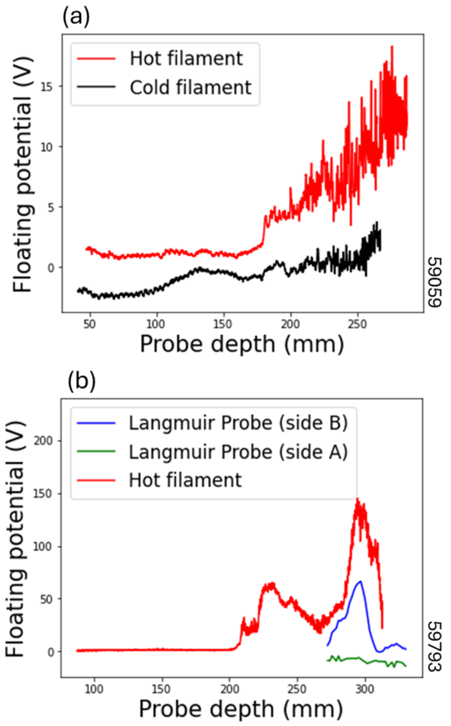

Fig. 4. (a) Comparison of the floating potentials measured by hot and cold filaments for a case with P_{Q1} = 500 kW, P_{Q2} = 0, and I_p = 700 kA. In this case, the probe does not plunge deep enough to capture the full plasma potential profile up to the edge of the ICRF antenna limiter. (b) Comparison of the floating potential measured by a hot filament and the Langmuir probes for a case with P_{Q1} = 500 kW, P_{Q2} = 100 kW, and I_p = 500 kA.

4 Plasma Potential's Dependence on Antenna Electrical Settings

When the plasma conditions are kept the same, the measured plasma potential scales linearly with the RF voltage at the strap feeding ports, or roughly like the square root of the coupled ICRF power, consistent with earlier Alcator C-Mod measurements [14]. More precisely, the plasma potential was most sensitive to the RF voltage measured at the upper right strap of the Q1 antenna (V_{ur1}), which is closest to where the probe connects magnetically. A comparison between two cases with different RF voltages is shown in Figure 5.

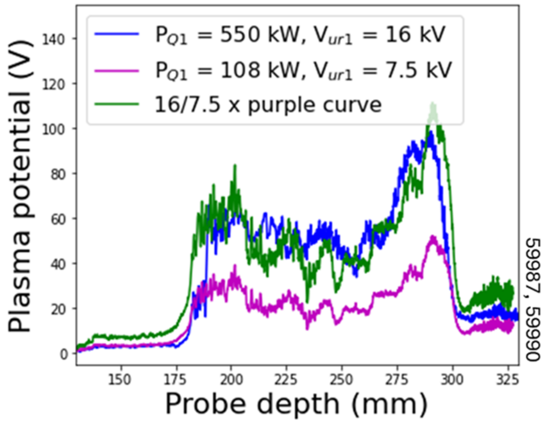

Fig. 5. Plasma potential profiles measured for two different values of V_{ur1}. The SOL density profile is the same for these two cases. The plasma potential scales linearly with V_{ur1}. The Q2 antenna was not powered in these shots.

Unsurprisingly, the plasma potential is smallest for a toroidal phasing between the straps of 180° (so-called dipole phasing), as shown in Figure 6(a). This is consistent with W sputtering also being minimized with dipole phasing [15]. An interesting observation is that the plasma potential profiles in this case exhibit a double-peak feature. The two peaks roughly correspond to the two times the field lines coming from the probe intercept the leading edge of the ICRF antenna limiter (Figure 6(b) and (c)). This interpretation is supported by the fact that only the first peak responds to changes in the antenna's left/right power ratio (Figure 7): at fixed coupled ICRF power P_{tot}, the amplitude of the first peak increases with P_{left}/P_{tot}, while that of the second peak remains unchanged. This is because the field lines corresponding to the first peak connect only to the left side limiter of the antenna, where the RF voltage is most sensitive to the power from the left straps. On the other hand, the field lines for the second peak pass in front of the two side limiters, thus being influenced by the RF voltage on both limiters, and by extension both straps. This is reminiscent of earlier measurements on ASDEX-Upgrade, where tungsten sputtering on the limiters of the two-strap antennas depended on the left/right power balance only for tiles that were not magnetically connected to the opposite side of the antenna [16].

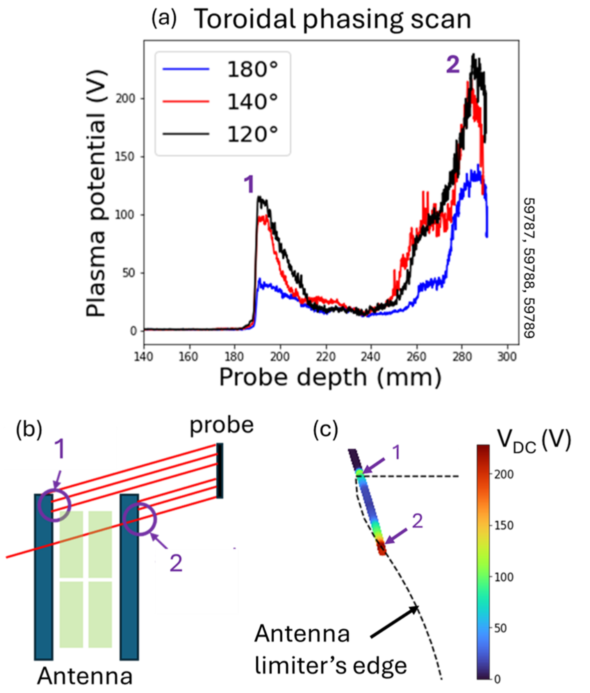

Fig. 6. (a) Plasma potential profiles measured during a scan of the toroidal phasing between the straps for P_{Q1} = 500 kW, P_{Q2} = 100 kW, and I_p = 550 kA. The effect of 100 kW from Q2 on the plasma potential was found to be negligible in this experiment. The two plasma potential peaks are observed even when only the Q1 antenna is powered. (b) Schematic representation of the probe's magnetic connection to the Q1 antenna, showing the field lines corresponding to the two peaks. (c) Projection of one of the plasma potential profiles in (a) (phasing of 120°) onto the right-side limiter of the Q1 antenna. The positions of the two peaks relative to the antenna limiter's leading edge are shown.

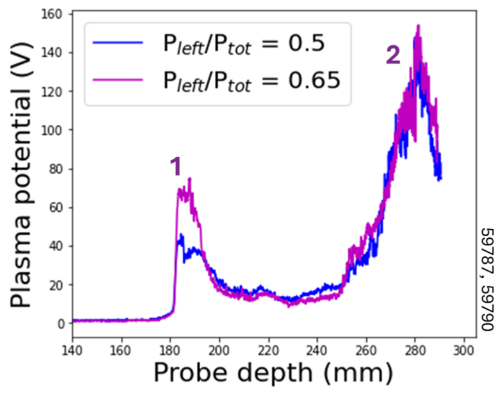

Fig. 7. Plasma potential profiles measured during a scan of the left/right power balance between the straps for P_{Q1} = 500 kW, P_{Q2} = 100 kW, and Ip = 550 kA. In the label, P_{left} is the power coupled through the left straps of Q1 and P_{tot} is the total power coupled through Q1.

5 Plasma Potential's Dependence on Other Plasma Parameters

One of the most reproducible observations in the collected dataset is that the ICRF-enhanced plasma potential decreases when the density at the antenna limiters increases, as shown in Figure 8. This behavior is only observed in "conventional" scenarios where the density at the antenna limiter exceeds the lower hybrid resonance density (S = 0 in Stix dielectric tensor notation, and approximately 9-11×10^{16} m^{-3} for typical WEST parameters). It confirms earlier measurements from Tore Supra, where the ICRF-enhanced floating potential measured by standard Langmuir probes was also found to decrease with increasing SOL density [11].

Of course, as the SOL density rises at fixed coupled ICRF power, the coupling resistance increases and the antenna voltage decreases. For the case shown in Figure 8, comparing the red and blue curves, V_{ur1} decreases by only about 12%, while the plasma potential decreases by a factor of 2. This indicates that the edge density is playing a major role in decreasing the plasma potential, since at fixed density, V_{DC} is proportional to V_{ur1} (Figure 5).

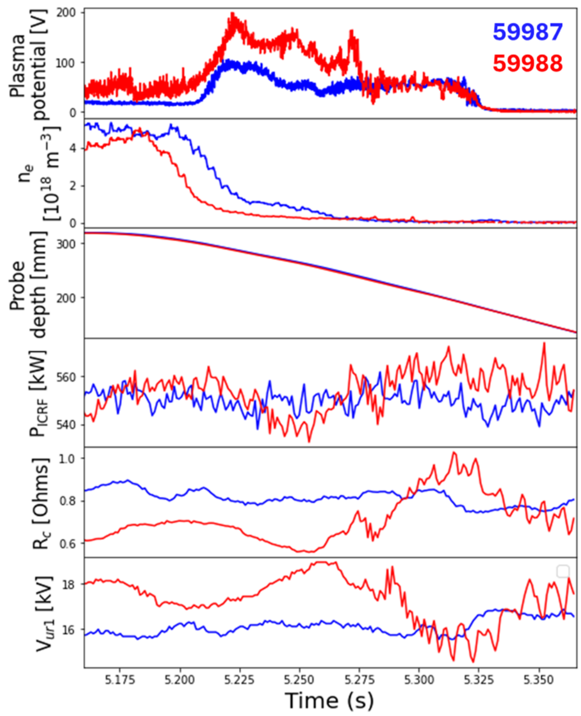

Fig. 8. Time trace of the plasma potential and edge density measured by the emissive and Langmuir probes during a plunge in two discharges with different edge densities. Only the Q1 antenna was powered in this case. The total coupled ICRF power P_{ICRF}, coupling resistance R_c, and RF voltage at the upper right strap of Q1 V_{ur1} are also shown. The probe depth shown in the figure is that of the emissive probe. Note that the Langmuir probes used to measure the density profile are located 18 mm deeper into the plasma than the emissive probe (see, for example, Figure 1).

The plasma potential's sensitivity to the edge density is especially visible in scenarios with strong MHD activity, in which particles and energy are periodically expelled from the core to the edge. This causes the edge density and antenna voltage to oscillate over fast time scales, leading to fast oscillations in the plasma potential: at approximately fixed coupled power, V_{DC} decreases as the antenna voltage decreases or the edge density increases (Figure 9). Again, the plasma potential can change by more than a factor of 2 when the antenna voltage only changes by about 10–20%, which points to the role of the edge density in determining the plasma potential.

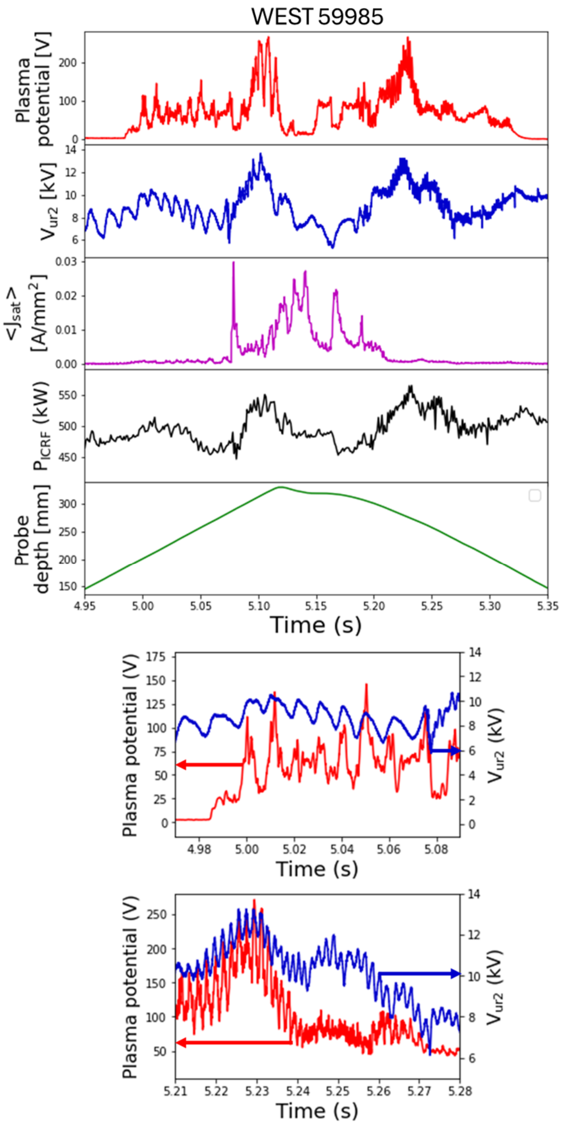

Fig. 9. Emissive probe measurement in a plasma with strong MHD activity, where the edge density and antenna voltage vary over fast time scales. The ICRF-enhanced plasma potential oscillates synchronously with the antenna voltage, and in the opposite way as the edge density. The average of the ion saturation current densities on both sides of the probe head <J_{sat}> is used as a proxy for the edge density. Only the Q2 antenna was powered in this shot, with the coupled power remaining close to 500 kW. The antenna voltage shown is that of the upper right strap of Q2, V_{ur2}, since it exhibits particularly strong variations in this case. The two plots at the bottom zoom over some areas from the plot at the top.

Finally, note that all previous results discussed in this paper compared cases with the same minority fraction H/(H+D). In general, the plasma potential measured by the probe tends to increase when the minority fraction shifts in the direction of weaker single-pass absorption of the waves. In Figure 10, four cases with increasing H/(H+D) are compared. The wave frequency is about 55 MHz, and the plasma current is 700 kA. These cases have similar edge density and V_{ur1}, but the plasma potential increases as H/(H+D) exceeds 5%, which coincides with a degradation in ICRF heating performance. We hypothesize that the weaker single-pass absorption at high H/(H+D) enhances the waves' interaction with the plasma edge, which could explain the larger plasma potential. An effort was made to measure the RF fluctuations picked up by the Langmuir probe installed on side B of the reciprocating probe head. To do so, the signal from the probe was split: one channel was used for the usual "DC" measurements of electron density and temperature, and the other was connected to a DC block, a 55 MHz bandpass filter, and a logarithmic RF power detector. Only the portion of the signal where the probe measures the ion saturation current was used for the RF measurement. The RF power detected by the probe is shown at the bottom of the top plot of Figure 10 and clearly increases when H/(H+D) exceeds 5%, suggesting a stronger RF interaction at the probe location. A noteworthy observation is that the probe is located near the hydrogen minority cyclotron layer at the top of the machine, a region where mode converted waves may be present. This could explain the sensitivity of the wavefield to H/(H+D) at this location. Whether the enhanced plasma potential measured by the emissive probe is primarily due to stronger RF rectification occurring at the antenna or locally at the probe remains an open question and will have to be investigated with dedicated modeling.

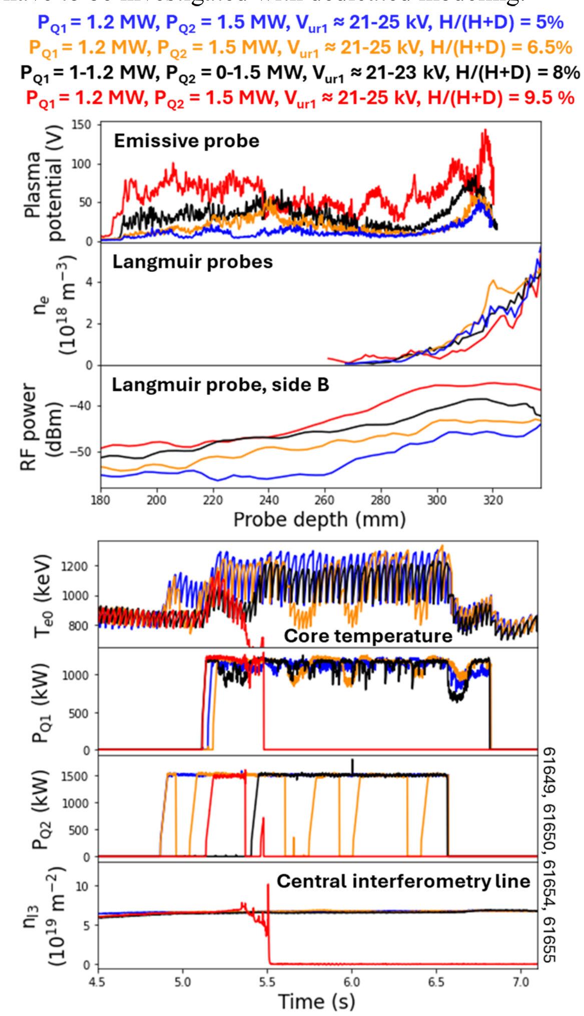

Fig. 10. (Top) Plasma potential and density profiles measured in four discharges with increasing H/(H+D). Also shown is the RF power (around 55 MHz) picked up by the Langmuir probe on side B of the probe head. The relevant ICRF parameters during the probe measurements are shown on top of the plot. (Bottom) Time traces from these four discharges suggesting a decrease in ICRF heating performance as H/(H+D) increases beyond 5%. The probe measurement is taken some time between t = 5.1 s and t = 5.6 s. The plasma current is 700 kA. For the case with H/(H+D) = 9.5% (red), the plasma cools down, then disrupts at t = 5.5 s.

6 Two-Dimensional Mapping of the Plasma and Floating Potentials

In order to reveal the spatial distribution of the plasma potential around the WEST ICRF antennas, an effort was made to map it in a 2D R-Z plane. This was achieved by scanning the plasma current from 450 kA to 650 kA in steps of 50 kA, thereby modifying the magnetic connection between the probe and the antennas. For each current value, the probe was plunged into the plasma, sampling a different region in R-Z space when mapped to the right-side limiter of the Q1 antenna, as shown in Figure 11(a). Note that centimeter-level imprecisions exist in the magnetic equilibrium reconstruction, though efforts were made to improve it by constraining it with interferometry measurements.

During the probe plunges, 500 kW was coupled through Q1 and 100 kW through Q2. In this experiment, the effect of P_{Q2} = 100 kW on the plasma potential was found to be negligible. This small amount of power was applied to Q2 to prevent a pressure increase inside the antenna caused by the multipactor effect [17], which would have prevented ramping up P_{Q2} later in the discharge to monitor W sputtering (Q2 being the only ICRF antenna that is monitored by visible spectroscopy). Since the edge density also affects the plasma potential, the current scan from 450 kA to 650 kA was performed at fixed Greenwald fraction to keep the SOL density approximately constant. Consequently, the antenna voltage showed little variation ($V_{url} \approx 15.5 - 17.5$ kV) despite the varying plasma current.

By interpolating between the measured profiles, a 2D map of the plasma potential was constructed, as shown in Figure 11(b). Using an additional reciprocating Langmuir probe located in port Q3A (see Figure 2), an even larger map of the floating potential was obtained, shown in Figure 12. A shot at 700 kA was added to complete the plasma potential map but was not used for the floating potential map. This shot had a 10–20% higher Greenwald fraction but much higher RF voltage and coupled power than the others ($V_{url} \approx 27$ kV, $P_{Q1} \approx 1.72$ MW, $P_{Q2} \approx 100$ kW). Over the entire database, V_{DC} was never higher than about 80 V when I_p = 700 kA, except for the case shown in Figure 10 with large H/(H+D).

The peaks in both the plasma and floating potentials are located near the corners of the antenna box, where high heat fluxes and tungsten sputtering are typically observed [10]. Antenna corners have been identified as regions of strongest ICRF-wall interaction in many devices with various antenna designs (see, for example, [2,12], as well as the discussions and references in [1]). This can be attributed to a large parallel component (relative to the background DC magnetic field) of the RF image currents at the antenna corners. Radially, the plasma and floating potentials peak near the leading edge of the ICRF antenna limiters. A possible explanation is that sheath rectification is strongest in the private part of the antenna limiters, and the plasma potential expands across the field lines and to the other side of the limiter due to perpendicular exchange of DC currents [3]. Hence, from the perspective of the probe, located outside the antenna, the plasma potential appears to peak at the antenna limiter's leading edge. In [18], it was shown through simulations that, for the cases presented in this section, the plasma potential on the antenna limiters is insensitive to the magnetic field line tilt angle. Hence, the experimentally constructed 2D map can be considered a realistic "snapshot" of the plasma potential.

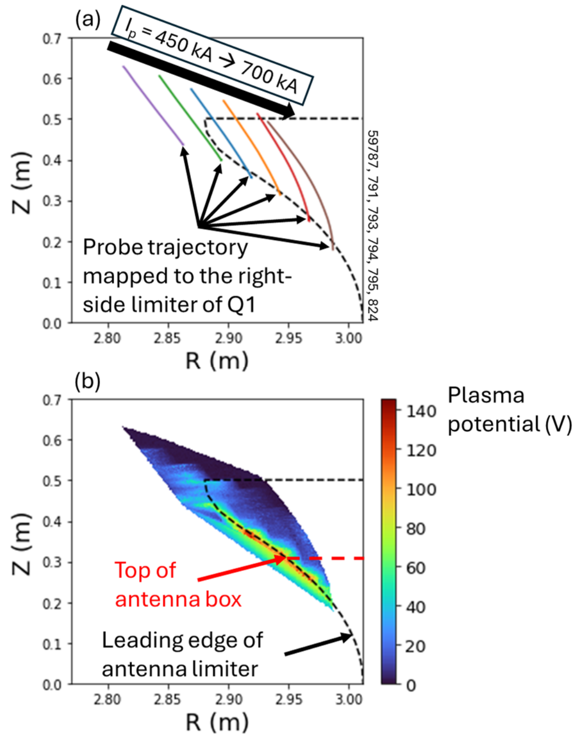

Fig. 11. (a) Emissive probe's trajectory mapped to the right-side limiter of the Q1 ICRF antenna for different values of the plasma current I_p going from 450 kA to 700 kA in 50 kA increments. (b) 2D map of the plasma potential interpolated from the emissive probe measurements.

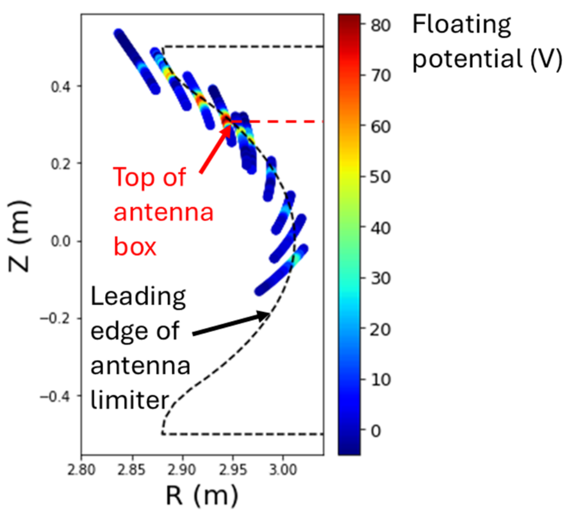

Fig. 12. Mapping of the floating potential profiles measured by the reciprocating Langmuir probes at ports Q3A and Q4B to the right-side limiter of the Q1 ICRF antenna. The data used is that of the I_p scan from 450 kA to 650 kA at fixed Greenwald fraction.

7 Conclusion

A large database of plasma potential profiles was assembled on the WEST tokamak using reciprocating emissive probes magnetically connected to two ICRF antennas. This paper summarized a first set of measurements aiming to characterize the plasma potential's dependence on other plasma parameters and antenna electrical settings under "standard" operating conditions, where the density at the antenna limiter exceeds the lower hybrid resonance density (S = 0). Special effort was made to map the plasma and floating potentials in 2D around the top half of the Q1 antenna, revealing a peak near the corner of the antenna box and radially close to the leading edge of the limiter. As part of a new ITPA-DivSOL task, the collected dataset will be used to quantitatively validate RF simulation tools capable of predicting rectified potentials via some version of the sheath boundary condition developed by Myra and D'Ippolito [7].

Additional experiments exploring ICRF antenna operation, RF sheath excitation, and plasma-wall interaction in the "low-density regime," where the lower hybrid resonance is located in front of the antenna, have also been conducted and will be reported separately.

This work was supported by U.S. Department of Energy award number DE-SC0014264. R. Diab would like to thank the entire WEST team for operating the machine and allowing him to plunge the probe during the many days of data collection for this project. R. Ochoukov is also gratefully acknowledged for his comments and suggestions on the safe operation of the emissive probes, and for first implementing the emissive probe drives on Alcator C-Mod, which were later refurbished for this project.

References

1. L. Colas et al., The geometry of the ICRF-induced wave–SOL interaction. A multi-machine experimental review in view of the ITER operation, Nucl. Fusion **62**, 016014 (2022). https://doi.org/10.1088/1741-4326/ac35f9
2. R. Diab et al., Mitigation of ICRF—edge plasma interaction in Alcator C-Mod, Nucl. Fusion **65**, 076038 (2025). https://doi.org/10.1088/1741-4326/ade456
3. J. Jacquot et al., Radio-frequency sheaths physics: Experimental characterization on Tore Supra and related self-consistent modelling, Phys. Plasmas **21**, 061509 (2014). https://doi.org/10.1063/1.4884778
4. S. Shiraiwa et al., Magnetic potential based formulation for linear and non-linear 3D RF sheath simulation, Nucl. Fusion **63**, 026024 (2023). https://doi.org/10.1088/1741-4326/aca6f9
5. W. Tierens et al., Radiofrequency sheath rectification on WEST: application of the sheath-equivalent dielectric layer technique in tokamak geometry, Nucl. Fusion **64**, 126039 (2024). https://doi.org/10.1088/1741-4326/ad80a9
6. C. Migliore et al., Using the Stix finite element RF code to investigate operation optimization of the ICRF antenna on Alcator C-Mod, Nucl. Fusion **63**, 106006 (2023). https://doi.org/10.1088/1741-4326/acee11
7. J. R. Myra, A tutorial on radio frequency sheath physics for magnetically confined fusion devices, J. Plasma Phys. **87**, 905870504 (2021). https://doi.org/10.1017/S0022377821000878
8. R. Ochoukov et al., ICRF-enhanced plasma potentials in the SOL of Alcator C-Mod. Plasma Phys. Control. Fusion **56**, 015004 (2014). http://dx.doi.org/10.1088/0741-3335/56/1/015004
9. T. Batal et al., Thermal and structural analysis of a new WEST reciprocating probe head with Titanium-Zirconium-Molybdenum armour material, Fusion Engineering and Design **217**, 115123 (2025). https://doi.org/10.1016/j.fusengdes.2025.115123
10. G. Urbanczyk et al., Perspective of analogy between heat loads and impurity production in L-mode discharges with ICRH in WEST, Nuclear Materials and Energy **26**, 100925 (2021). https://doi.org/10.1016/j.nme.2021.100925
11. M. Kubič et al., Attenuation of ICRH-induced potentials in the SOL of Tore Supra. AIP Conference Proceedings **1406**, 215 (2011). https://doi.org/10.1063/1.3664963
12. M. Kubič et al., Measurement of sheath potential in RF-biased flux tubes using a retarding field analyzer in Tore Supra tokamak. Journal of Nuclear Materials **438**, S509 (2013). http://dx.doi.org/10.1016/j.jnucmat.2013.01.105
13. J. P. Gunn, Evidence for strong secondary electron emission in the tokamak scrape-off layer. Plasma Phys. Control. Fusion **54**, 085007 (2012). http://dx.doi.org/10.1088/0741-3335/54/8/085007
14. S. J. Wukitch et al., ICRF specific impurity sources and plasma sheaths in Alcator C-Mod. Journal of Nuclear Materials **390** (2009) 951–954. https://doi.org/10.1016/j.jnucmat.2009.01.245
15. J. Hillairet et al., WEST actively cooled load resilient ion cyclotron resonance heating system results. Nucl. Fusion 61, 096030 (2021). https://doi.org/10.1088/1741-4326/ac1759
16. V. Bobkov et al., Progress in controlling ICRF-edge interactions in ASDEX Upgrade, AIP Conf. Proc. **1689**, 030004 (2015). https://doi.org/10.1063/1.4936469
17. E. Al Hajj Sleiman et al., Multipactor predictions for ion cyclotron resonance heating antennas of the tokamak WEST, Nucl. Fusion **63**, 126054 (2023). https://doi.org/10.1088/1741-4326/ad0509
18. G. Urbanczyk et al., ICRF near-field effects sensitivity to magnetic tilt-angle, 25th Topical Conference on Radio-Frequency Power in Plasmas, Schloss Hohenkammer, Germany, May 19-22 (2025)